Cao *et al. Chin. J. Mech. Eng.* (2018) 31:48
https://doi.org/10.1186/s10033-018-0247-0

Chinese Journal of Mechanical Engineering

ORIGINAL ARTICLE

Open Access

Influence of Endwall Boundary Layer Suction on the Flow Fields of a Critically Loaded Diffusion Cascade

Zhi-Yuan Cao[1,2*], Bo Liu[1] and Ting Zhang[3]

Abstract

Boundary layer suction is an effective method used to delay separations in axial compressors. Most studies on boundary layer suction have focused on improving the performance of compressors, whereas few studies investigated the influence on details of the flow fields, especially vortexes in compressors. CFD method is validated with experimental data firstly. Three single-slot and one double-slot endwall boundary layer suction schemes are designed and investigated. In addition to the investigation of aerodynamic performance of the cascades with and without suction, variations in corner open separation, passage vortex, and concentration shedding vortex, which are rarely seen for the flow controlled blades in published literatures, are analyzed. Then, flow models, which are the ultimate aim, of both baseline and aspirated cascades are established. Results show that single-slot endwall suction scheme adjacent to the suction surface can effectively remove the corner open separation. With suction mass flow rate of 0.85%, the overall loss coefficient and endwall loss coefficient of the cascade are reduced by 25.2% and 48.6%, respectively. Besides, this scheme increases the static pressure rise coefficient of the cascade by 3.2% and the flow turning angle of up to 3.3° at 90% span. The concentration shedding vortex decreases, whereas the passage vortex increases. For single-slot suction schemes near the middle pitchwise of the passage, the concentration shedding vortex increases and the passage vortex is divided into two smaller passage vortexes, which converge into a single-passage vortex near the trailing edge section of the cascade. For the double-slot suction scheme, triple-passage vortexes are presented in the blade passage. Some new vortex structures are discovered, and the novel flow models of aspirated compressor cascade are proposed, which are important to improve the design of multi-stage aspirated compressors.

Keywords: Axial-flow compressor, Diffusion cascade, Flow separation, Corner separation, Boundary layer suction, Passage vortex

1 Introduction

With increasing design requirements of thrust-weight ratio and efficiency of modern aero-engines, the total pressure ratio per stage of axial flow compressors increases [1, 2]. To increase total pressure ratio per stage, designers often utilize high blade loading [2, 3]. However, high blade loading results in highly three-dimensional (3D) phenomena inside the compressors.

Despite rapid development of optimization methodologies utilized in turbomachinery [4, 5], diffusion factors higher than 0.6 are rarely suggested during the actual design process. 3D flows, such as clearance vortex, horseshoe vortex, and separations, are inevitable in highly-loaded compressors [6]; and it can probably result in the degradation of aerodynamic performance and fluid-structure problems [7]. In particular, flow fields in the suction surface/endwall corner region are observed as 3D corner separation [8, 9]. Under off-design operating conditions, the corner separation increases rapidly and deteriorates compressors significantly. Auchoybur et al. [8], introduced a novel method for controlling endwall flow fields; in this method, the endwall velocity triangles

*Correspondence: zycao@pku.edu.cn
[1] School of Power and Energy, Northwestern Polytechnical University, Xi'an 710072, China
Full list of author information is available at the end of the article

were tailored. It's shown that the operating range of a compressor blade row was mainly dependent on the size and structure of the endwall inlet boundary layer, not the geometry near the endwall of the blade row. However, the blade row investigated was stacked three dimensionally; as such, the effect of bowed blade on controlling endwall flow could not be excluded. Taylor et al. [10], utilized a novel method to design bowed blade for controlling corner separation. The corner separation was delayed while the transverse pressure gradient remained unchanged. This study showed that passive control method can effectively reduce the corner separation, but the loading of the investigated compressors was low. In highly loaded compressors, passive control method exerts limited effect.

Aspiration, also known as boundary layer suction, was put forward first by Kerrebrock in 1997 and has been used in experimental compressors to increase blade loading while avoiding large flow separation [11–13]. Merchant [14] discussed the impact of boundary layer suction on the aerodynamic design and performance of blade profile. The important blade design features were also characterized to achieve high loading and minimize the aspiration requirement. Two aspirated compressors were designed and investigated using CFD method; these compressors achieved high loading over most of the blade span. A transonic aspirated compressor stage was designed and experimentally investigated to demonstrate the application of boundary layer suction [15]. The compressor stage achieved the maximum pressure ratio of 1.58 and efficiency of 90% at the design point with a tip speed of 228.6 m/s. The aspiration for the stage was 0.5% of the inlet mass flow on both the suction surface of the rotor and stator. This paper also presented time-accurate and ensemble-averaged flow fields. Another aspirated fan stage was designed to achieve a pressure ratio of 3.4 at 457.2 m/s [16]. The fan stage pressure ratio was more than 3 at the design speed in the experiment, with an aspiration flow fraction of 3.5%. Only flow fields on the S1 surface were presented in the paper. Bronwyn et al. [17] designed a highly-loaded aspirated cascade by using the pressure-recovery concept and reported an airfoil with a Leiblien Diffusion Factor of 0.71. References [18–23] also investigate the application of boundary layer suction in compressors.

Gbadebo et al. [24, 25], investigated the natural of 3D separations in axial compressors; based on the insights gained regarding the formation of separations, typical compressor stator hub corner 3D separation was controlled and eliminated by boundary layer suction by up to 0.7% of the inlet mass flow [26]. Experimental investigation was also performed to confirm the removal of the separated region from the blade suction surface. The results indicated that the blade exhibits increased loading, enhanced averaged static pressure rise, and uniform exit flow. Chen et al. [27] performed active control of corner separation by boundary layer suction and investigated the influence of the location of the endwall suction slot. Cao et al. [28] investigated partial span suction on the suction surface of a diffusion cascade, and then removed both the trailing edge separation and corner separation through coupled suction surface and endwall suction.

Previous investigations were focused on improving the compressor performance or controlling separations. The influence of aspiration on flow fields, especially vortex structures, has been rarely studied. In multi-stage compressors, the vortexes of the upstream blade rows, such as horseshoe vortex, passage vortex, and concentration shedding vortex, may significantly influence the flow field of downstream blade rows. Therefore, flow fields, especially vortexes, in the aspirated compressors must be elucidated.

Based on the previous analysis, a critically loaded diffusion cascade with endwall boundary layer suction was investigated numerically. The influence of endwall suction on vortexes in the cascade was determined, and flow models were established for both baseline and aspirated cascades.

2 Diffusion Cascade Descriptions

The diffusion cascade is a subsonic critically loaded compressor cascade with weak trailing edge separation at the mid-span and 3D separation in the suction surface/endwall corner. The design inlet Mach number is 0.6, and the incidence angle is 0.5°. Table 1 shows the key parameters of the cascade.

3 Numerical Method and Validations

The 3D numerical simulation was conducted on a single cascade passage on the assumption of periodicity. Structure grid was created by AUTOGRID of NUMECA FINE/TURBO in the cascade passage. The total grid number of the baseline cascade is about 1.03

Table 1 Main geometry parameters of the cascade

Geometry parameters of the cascade	Data
Chord c (m)	0.063
Blade height h (m)	0.10
Setting angle γ (°)	15.40
Inlet blade angle β_{1k} (°)	40.17
Outlet blade angle β_{2k} (°)	− 13.21
Solidity τ	1.66
Maximum thickness/chord	0.08
Maximum thickness position/chord	0.61

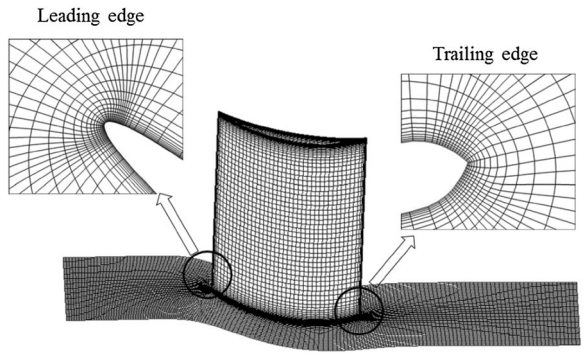

Figure 1 Mesh near the blade surface and endwall

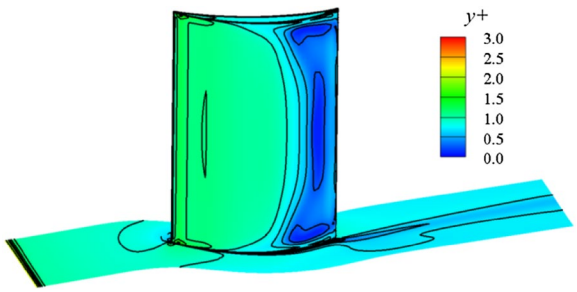

Figure 3 *y*+ contours near the endwall and blade surface

million. The mesh near the blade surface and endwall is shown in Figure 1. "O" type grid was created near the blade surface to obtain high mesh quality. "H" type grid was created for the endwall boundary layer suction slot by IGG. The grid of the suction slot was connected to the cascade passage by full non-matching connection technology.

The validation of grid independence is shown in Figure 2, in which static pressure ratio and loss coefficients are illustrated. The static pressure ratio and the loss coefficient were normalized by the values calculated at the grid number of 1.03 million. π_N is the normalized static pressure ratio, while Cp^*2_N is the normalized loss coefficient. The static pressure ratio and loss coefficient relatively vary when the total grid number is lower than 1 million. Although the static pressure ratio and loss coefficient change with increasing mesh density, as the total grid number is higher than 1 million, the variations are small. Therefore, mesh density utilized in the paper is appropriate. The linear cascade was numerically simulated by FINE/TURBO software. S-A turbulence model was utilized in the calculation. Inlet total pressure, inlet total temperature, inlet flow angle, and outlet static pressure were presented at the boundary according to the experimental data [28]. Figure 3 shows the *y*+ contours near the end wall and blade surface, which meet the requirements recommended by NUMECA User Manual [29] for the S-A model. Thus, the mesh is suitable for the turbulent model utilized.

Figure 4 compares the mid-span static pressure coefficient (Cp) of the experimental and numerical results for the baseline cascade. Equation (1) expresses the definition of Cp, as shown in the following:

$$Cp = \frac{P}{P_1^*}, \tag{1}$$

where P is the local static pressure, P_1^* is the inlet total pressure. Cz is the axial chord of the cascade, and z is the axial direction. It's indicated that the numerical results show excellent agreement with the experiment results.

The experimental result of NACA 64A-905 cascade from American Air Force Institute of Technology [30] was utilized in this paper. Figure 5 compares the suction surface flow field between experimental and numerical

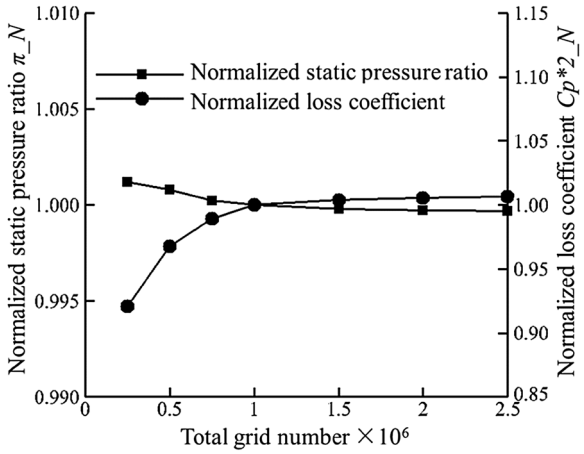

Figure 2 Validation of grid independence

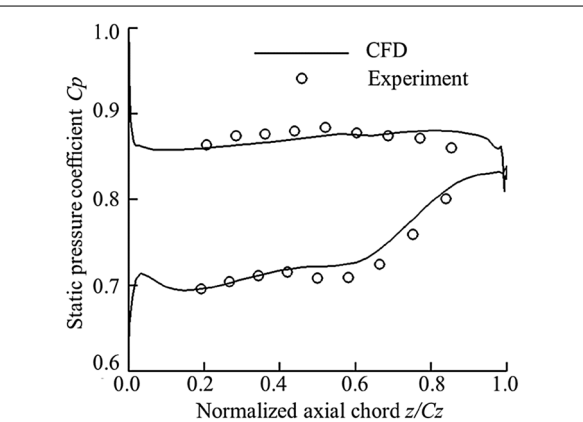

Figure 4 Comparison of *Cp* of baseline cascade [28]

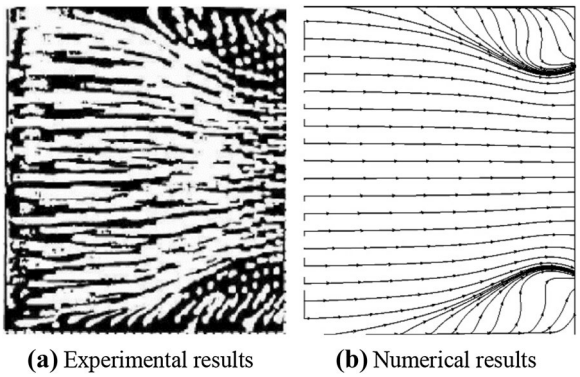

Figure 5 Comparison of near-wall flow field of NACA 64A-905 cascade [30]

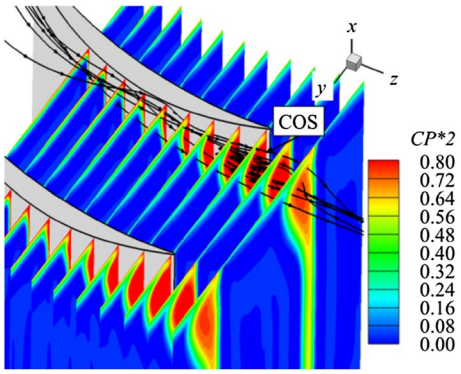

Figure 7 Loss coefficient contours at different axial sections and 3D streamlines

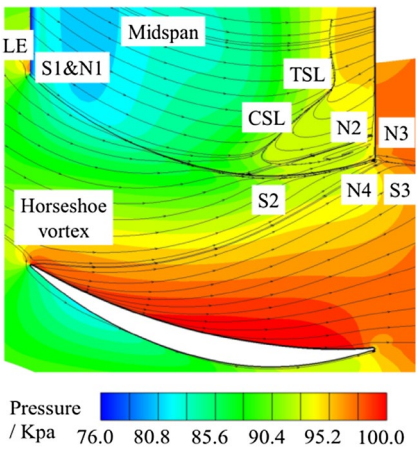

Figure 6 Static pressure contour/limiting streamlines

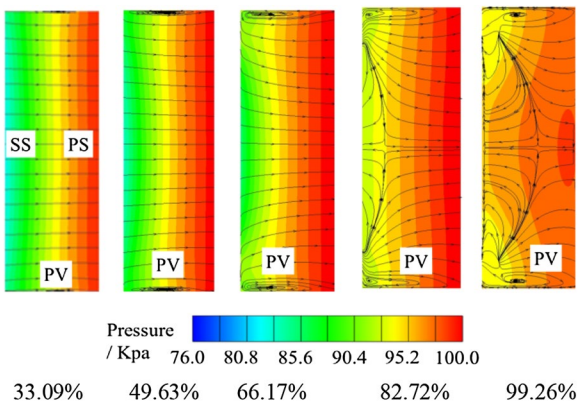

Figure 8 Numerical simulated results of S3 surfaces at different axial chord positions

results. The limiting streamlines of numerical results show great agreement with experiment results.

The flow fields of baseline cascade at design condition are shown in Figures 6, 7, 8. Figure 6 shows the static pressure contour/limiting streamlines on suction surface/endwall. Both corner separation line (CSL) and tailing edge separation line (TSL) are found on the suction surface of the cascade. The endwall boundary layer minimally influences the mid-span flow field than that on the near endwall region of the blade; as such, the TSL is closer to the trailing edge. TSL is mainly caused by the boundary layer of the suction surface. The corner separation line is farther from the trailing edge than that from the mid-span region.

The horseshoe vortex separates at the leading edge saddle point S1 on the endwall near the leading edge (LE). The suction surface side leg (HS) and the pressure surface side leg (HP) of the horseshoe vortex system originate from the saddle point S1. The HP moves toward the trailing edge of the adjacent blade under the cross-passage pressure gradient of the endwall. The HS intersects with the blade suction surface soon as it flows toward the surface of the blade under the cross-passage pressure gradient. As the low-momentum fluid between the HP and HS both concentrates to the endwall corner, 3D corner separation occurs.

Different with that of Refs. [19, 20], there is neither nodal point nor saddle point existing near the intersection of the HS and suction surface. The corner separation line originates from a normal point near the intersection position. The limiting streamlines derived from the saddle point S2 also join the corner separation line. Focus N2 in the 3D corner separation region of the suction surface.

Figure 7 shows the loss coefficient (CP^*2) contours at different axial sections and 3D streamlines of the baseline cascade. Equation (2) expresses the definition of CP^*2:

$$CP*2 = \frac{2(P_1^* - P^*)}{\rho_1 v_1^2}, \tag{2}$$

where P_1^* is the inlet total pressure, P^* is the local total pressure, ρ_1 is the inlet density, v_1 is the inlet velocity. The red region represents high loss coefficients and is mainly located in the suction surface/endwall corner. The 3D streamlines exhibit severe reverse flow in the corner, which indicates that the baseline cascade experiences corner open separation (COS).

The numerical results of the S3 surfaces of the baseline cascade are shown in Figure 8. The passage vortex(PV) begins at about 33.09% axial chords and is located at the middle pitchwise of the passage near the endwall. As the axial position of S3 surface goes downstream toward the trailing edge, the passage vortex enlarges and the vortex core moves to the suction surface.

4 Endwall Boundary Layer Suction Schemes

4.1 Single-Slot Suction Schemes

This paper designed three different single-slot endwall boundary layer suction schemes. The geometry of the slots was the same but differed in terms of the pitchwise position. The slots exhibited a width of 1 mm and were distributed from 12.4% to 84.0% axial chords. Each single-slot suction scheme had one slot on each endwall of the cascade. Both slots were located at the same position on the endwall. The boundary conditions of both suction slots were the same. The single-slot suction schemes are ESA, ESB, and ESC (Figure 9).

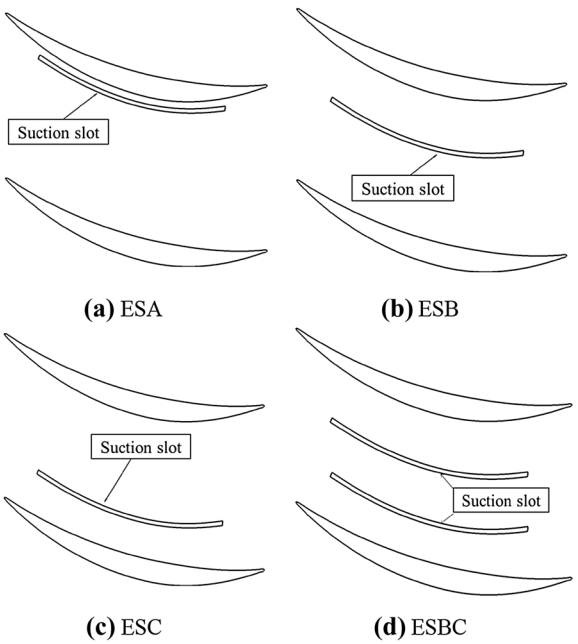

Figure 9 Endwall suction schemes

4.2 Double-Slot Suction Scheme

One double-slot endwall boundary layer suction scheme was investigated. The double-slot suction scheme was the combination of ESB and ESC (Figure 9(d)). The suction mass flow rate of each slot was the same with that of single-slot suction schemes.

4.3 Determination of Suction Slot and Suction Mass Flow Rate

Gbadebo et al. [24], recommended that the optimum slot should be close to the suction surface and sufficiently long to remove the limiting streamline; this slot should be positioned downstream the peak suction on the blade to near the trailing edge. However, in the actual application of endwall boundary layer suction, a suction slot located near the suction surface does not practically consider the structural strength. Thus, in the present study, the ESA scheme was located at some distance from the suction surface, i.e., 2 mm (the pitch is 37.95 mm). ESB and ESC schemes were designed at 12 mm and 24 mm from the suction surface, respectively, to investigate the pitchwise effect of the single slot. ESA, ESB, and ESC exhibited the same geometry but differed in terms of pitchwise location.

Three suction slots with different lengths for ESA scheme were studied to determine the length of the slot. The origin positions of the three suction slots were the same, i.e., 12.4% axial chord, near the peak suction on the blade [24]. The ending points were at 68.0%, 84.0%, and 100% axial chord, respectively. Schemes with three different suction slots are named as ESA-A, ESA-B, and ESA-C. The loss coefficients are compared in Figure 10. ESA-A exhibits the lowest loss coefficient under suction mass flow rates lower than 0.7% and the highest loss coefficient at higher suction mass flow rate. At suction mass flow rates higher than 0.7%, the loss coefficients of ESA-B and ESA-C are about the same and lower than that of

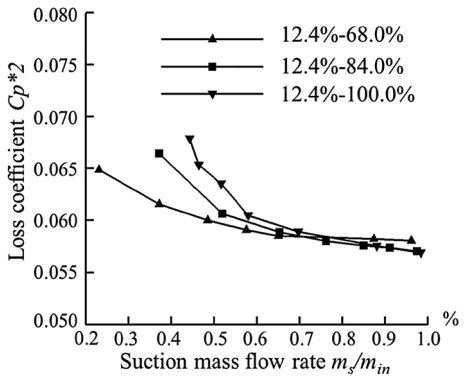

Figure 10 Loss coefficients for different suction slots

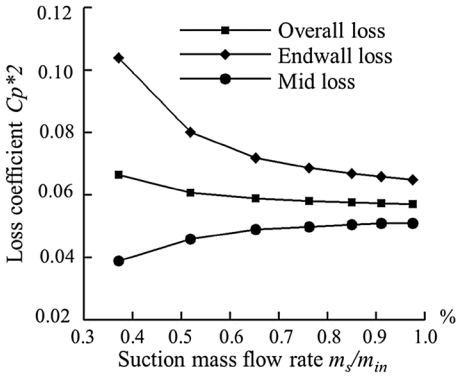

Figure 11 Variations of loss coefficient with suction mass flow rates

ESA-A. Hence, the suction slot ESA-B is sufficient to suck off low energy fluid near the suction surface/endwall corner. Considering that the cascade with a short slot is beneficial for structural strength, ESA-B was selected for further investigation. All the three suction slots of ESA, ESB, and ESC were distributed from 12.4% to 84.0% axial chord.

Figure 11 shows the variations in loss coefficients, namely, overall loss coefficient, end-wall loss coefficient, and mid-span loss coefficient, with suction mass flow rate. The endwall loss coefficient is defined as the loss of 20% mass flow near each endwall; the mid-span loss coefficient is defined as the loss of the other 60% mass flow at the mid-span [10]. With increasing suction mass flow, the endwall loss coefficient decreases, whereas the mid-span loss coefficient increases. The overall loss of the cascade reduces at the investigated suction mass flow rate range. The loss coefficients significantly vary when the suction mass flow rate is lower than 0.85%. At suction mass flow rates higher than 0.85%, the loss coefficients, especially the overall loss coefficient, almost do not change as the suction mass flow rate increases. Therefore, to compare the flow field of different endwall suction schemes at the same suction mass flow rate, the suction mass flow rate of each suction slot was 0.85%; and the overall and endwall loss coefficients are reduced by 25.2% and 48.6% at the suction mass flow rate, respectively. All the endwall suction schemes were conducted under the design inlet condition.

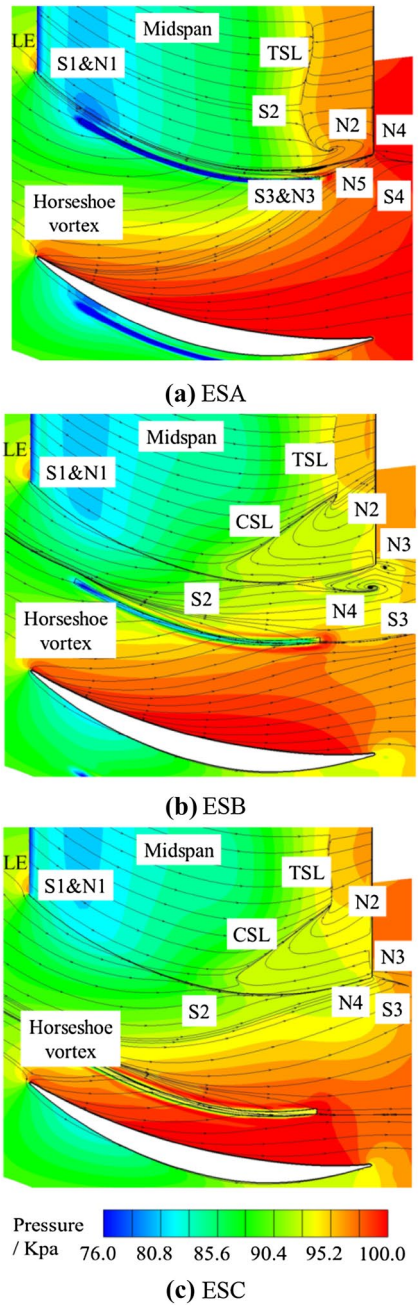

Figure 12 Suction surface/endwall streamlines and static pressure contour

5 Results and Discussions

5.1 Single-Slot Suction Schemes

Figure 12 shows the suction surface/endwall streamlines and static pressure contours of different single-slot suction schemes. ESA improves the cascade most in the three single-slot endwall suction schemes. The suction surface leg of the horseshoe vortex is sucked off by the endwall suction slot. HS no longer rolls up and intersects with the suction surface. The low-momentum fluid between HS and HP is almost removed by the endwall suction slot. Therefore, less low-momentum fluid is concentrated to the suction surface corner. Compared with that of the baseline cascade, the limiting streamlines on the suction surface do not contract to the mid-span. The

flow field in the cascade tends to be two dimensional. The separation line on the suction surface is distributed uniformly along spanwise. As a consequence, the 3D corner separation is almost eliminated by the ESA suction scheme. The focus point N2 emerges in the suction corner, where the trailing edge separation is terminated.

As the blockage in the corner is reduced, the aerodynamic area of cascade exit increases. The static pressure on the endwall and blade trailing edge increases significantly. The static pressure rise coefficient (*CP*2) of the entire cascade increases by 3.2%. Equation (3) expresses the definition of *CP*2:

$$CP2 = \frac{2(P_2 - P_1)}{\rho_1 v_1^2}, \tag{3}$$

where P_2 is the inlet total pressure, P_1 is the local total pressure, ρ_1 is the inlet density, v_1 is the inlet velocity. However, the flow field in the mid-span is deteriorated. The trailing edge separation line moves upstream because of weakened flow path concentrating effect in the mid-span of the baseline cascade after endwall suction. Further analysis on the flow path concentrating effect is presented in the following section.

In Figure 12(b), although endwall suction removes the low-momentum fluid between the HP and endwall suction slot, the flow field near the endwall of the cascade deteriorates. The pressure gradient between the suction slot and suction surface decreases. The curvature radius of the limiting streamlines on the endwall between the suction slot and suction surface increases obviously. The endwall cross-passage flow toward the suction surface reduces. However, reduced cross-passage flow does not improve the flow field in the corner. The originating point of the 3D separation almost remains unchanged, and the separation region on the suction surface minimally changes little. As the cross-passage static pressure gradient decreases, the low-momentum fluid does not have sufficient driving force to migrate along spanwise. Therefore, the low-momentum fluid concentrates at the endwall corner, and the two vortexes near the trailing edge significantly increase.

The suction slot of the ESC scheme is located far from the suction surface. The amount of low-momentum fluid is low near the slot; thus, the endwall cross-passage flow, 3D corner separation, and trailing edge separation almost remain unchanged. However, the saddle point S2 and nodal point N2 on the suction surface corner of the baseline cascade are eliminated after ESB and ESC endwall suction. After ESB and ESC suction, a saddle point S2 shows up near the intersection position of HS with the suction surface; this point is the onset point of the corner separation line.

Figure 13(a) shows the spanwise profile of pitchwise averaged exit flow angles. β_2 is the exit flow angle of the cascade. For baseline cascade, the exit flow angles near the end wall are negative, and the minimum angle is about minus 6°, which indicates the overturning of the flow near the endwall. This phenomenon is caused by the cross-passage flow near the endwall. At about 90% span, the flow angles show significant underturning, and the maximum angle is about 4.5° because of passage vortex and corner 3D separation.

The distribution of exit flow angles considerably varies after ESA suction. Near the endwall, the overturning of the flow angles increases, consistent with the increased endwall cross-passage flow in Figure 12(a). The exit flow angles of about 24% spans near the endwall decrease, indicating that the flow turning angles of the region increase. This finding agrees with the results of the elimination of corner 3D separation after ESA suction. At 50% to about 76% spans, the exit flow angles increase to about 0° as the trailing edge separation increases. When the exit flow angles increase to 0°, the exit flow area of the cascade increases to the maximum; this condition results in increased mid-span static pressure.

Other endwall suction schemes minimally influence the distribution of exit flow angles. The variations are

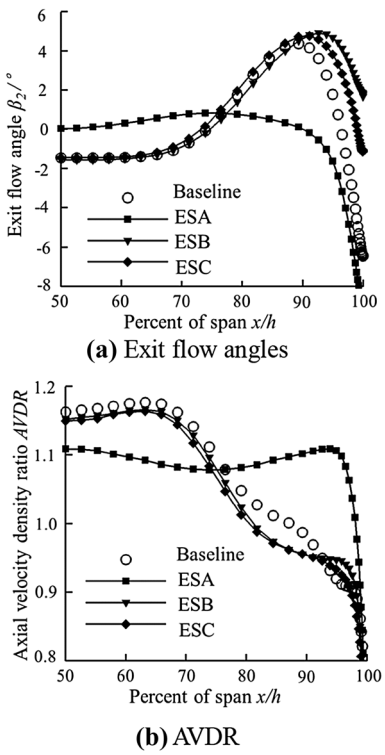

Figure 13 Spanwise profile of pitchwise averaged aerodynamic parameters

mainly near the endwall. The overturning of flow angles near the endwall decreases because these endwall suction schemes decrease the cross-passage pressure gradient near the end wall, especially between the suction surface and the suction slot. ESB increases the exit flow angles near the endwall most.

Figure 13(b) shows the spanwise profile of pitchwise mass flow averaged axial velocity density ratio (*AVDR*), which represents the blockage effect of the blade passage. Equation (4) expresses the definition of *AVDR*:

$$AVDR = \frac{\rho_2 v_{2a}}{\rho_1 v_{1a}}, \tag{4}$$

where ρ_2 is the outlet density, v_{2a} is the outlet velocity, ρ_1 is the inlet density, v_{1a} is the inlet velocity. At about 80%−100% span of the baseline cascade, *AVDR* is lower than 1, which indicates the presence of flow blockage near the endwall. At about 50%−80% span of the baseline cascade, *AVDR* is higher than 1, indicating that the flow near the endwall contracts to the mid-span because of the blockage of corner separation and endwall boundary layer. As a result of the fluid contraction, the aerodynamic exit area of the cascade is smaller than the geometry exit area. Therefore, the diffusion of the cascade mid-span is lower than that of the 2D cascades; moreover, the separation of mid-span is smaller than under 2D conditions.

After ESA endwall suction, the blockage near the end wall reduces significantly. The value of *AVDR* increases obviously at 76%−100% spans but decreases at 50%−76% spans. The spanwise profile of *AVDR* is more uniform than that of the baseline cascade; this finding indicates a reduced contracting effect of the endwall fluid toward the mid-span. Consequently, the diffusion loading near the mid-span increases significantly, resulting in increased static pressure and separation in the mid-span after ESA suction. Other endwall suction schemes have less influence on the *AVDR* distribution than ESA. The *AVDR* decreases minimally in 50% to about 94% span, similar to the results of the ESA suction scheme.

Figure 14 shows the loss coefficient contours at different axial sections and 3D streamlines in the suction surface/endwall corner.

In Figure 14(a), the red region in the suction surface/endwall corner of the ESA suction scheme reduces significantly. The 3D streamlines in the corner flow smoothly downstream, which indicates that the corner open separation (COS) is eliminated by ESA endwall suction. In Figure 14(b), the high loss region is larger than the baseline cascade; the reverse flow in the cascade corner is more severe than that in the baseline cascade, which demonstrates that the 3D corner open separation increases. As shown in Figure 14(c), the flow field of the ESC scheme is similar to that of the baseline cascade. The distribution of high loss region and the 3D corner open separation are similar.

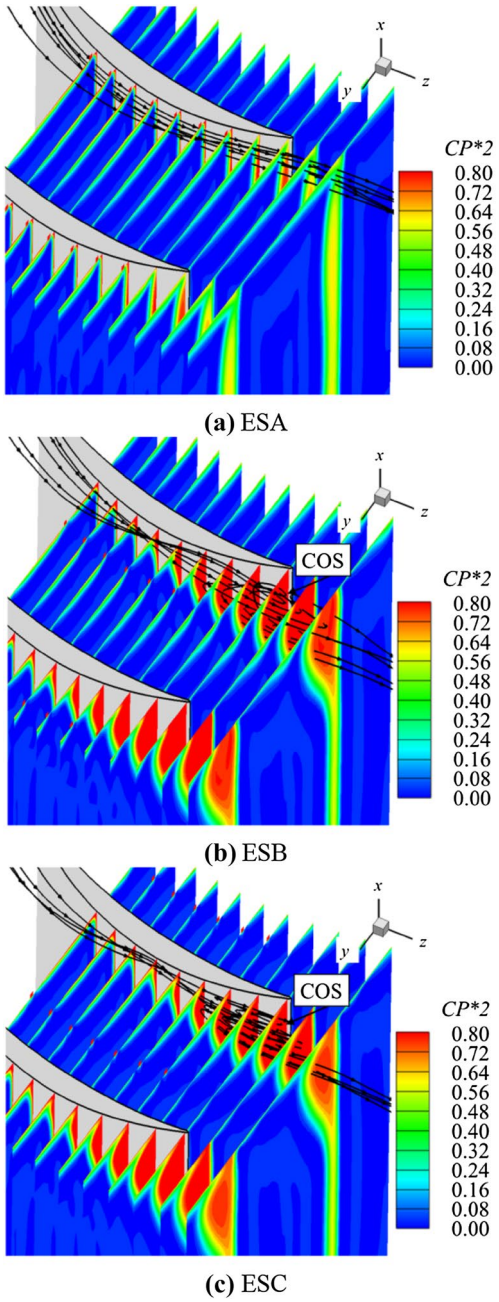

Figure 14 Loss coefficient contours at different axial sections & 3D streamlines

Figure 15 compares the velocity vector/Mach number contour of baseline cascade and single-slot suction schemes at the cascade outlet. Only the lower half span of the cascade passage is shown.

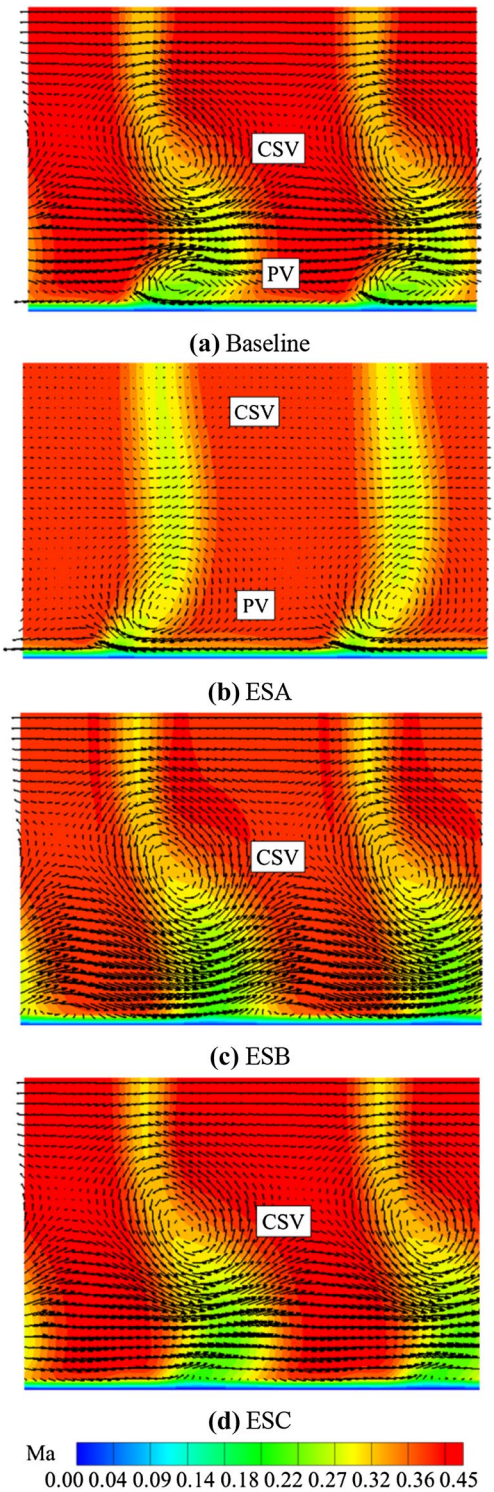

Figure 15 Velocity vector/Mach number contour at cascade outlet

Figure 15(a) presents the flow field of the baseline cascade. Corner open separation lead to the low Mach number region at the cascade outlet, located near the endwall. The low Mach number region is located on the right of the mid-span wake region and bends toward the right of the figure. This finding agrees well with the outlet flow angles in Figure 13(a). A passage vortex (PV) is present near the endwall, and a concentration shedding vortex (CSV) is located at about 25% span. The concentration shedding vortex is larger than the passage vortex. In Figure 15(b), the low Mach number region near the endwall reduces as the corner open separation is eliminated by ESA suction. The low Mach number region near the endwall moves toward the left of the figure under the enlarged cross-passage pressure gradient. As ESA suction increases the cross-passage pressure gradient near the endwall, the passage vortex increases. However, the concentration shedding vortex nearly vanishes. The Mach number contours in Figure 15(c) and (d) show similar variations. The low Mach number region near the endwall moves toward the right of the figure, indicating decreased cross-passage pressure gradient near the endwall. As the cross-passage pressure gradient reduces, the passage vortexes of ESB and ESC schemes at the cascade outlet vanish, resulting in increased concentration shedding vortex.

Figure 16 shows the static pressure/streamlines of different axial chords after ESB endwall suction. The novel phenomenon discovered is that the passage vortex is divided into two different vortexes. The first vortex is located on the left side of the suction slot and is called PVS because it is near the suction surface. The other vortex is located on the right side and called as PVP. The driving force of both PVS and PVP is the endwall cross-passage static pressure gradient; thus, the rotating directions of PVS and PVP are the same. PVS decreases as the double-passage vortexes flow downstream. PVS converges to PVP at about 115.8% axial chords, and then the double-passage vortexes are replaced by a single-passage vortex.

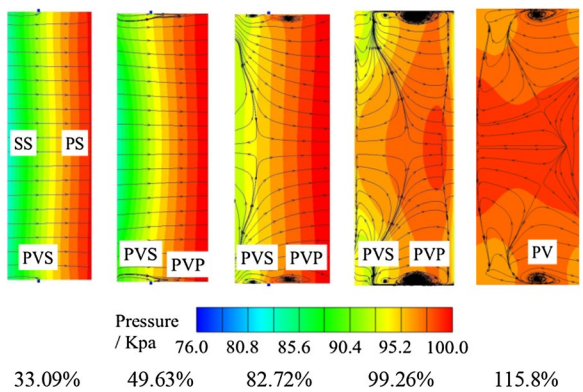

Figure 16 Static pressure contour/streamlines of different axial chords after ESB suction

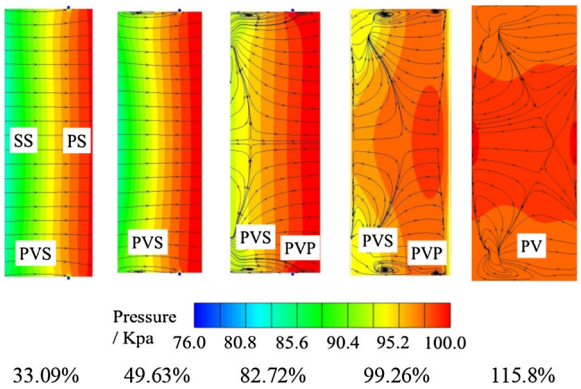

Figure 17 Static pressure contour/streamlines of different axial chords after ESC suction

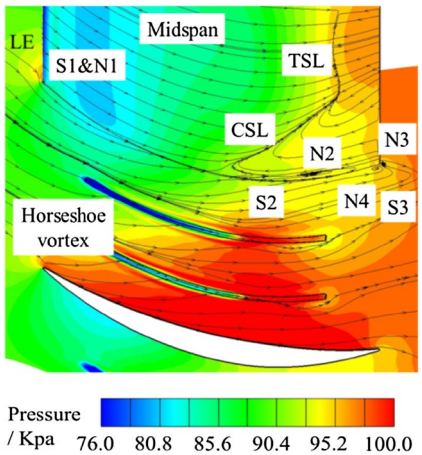

Figure 18 Suction surface/endwall streamlines and static pressure contour

The static pressure contours/streamlines of different axial sections after ESC suction is shown in Figure 17. The ESC suction scheme reduces the passage vortex. Before 49.63% axial chord, the region of passage vortex is between suction slot and suction surface. Similar to the ESB scheme, double-passage vortexes system is formed from about 82.72% axial chords. As the suction slot is close to the pressure surface, the space for the development of PVP is small. Therefore, the PVP is smaller than PVS. As the double-passage vortexes flow downstream, they combine into a single-passage vortex about 115.8% axial chords. The single-passage vortex disappears during dissipation with the bulk flow.

5.2 Double-Slot Suction Scheme

In the previous section, significant variations in flow fields were discovered after single-slot endwall suction, especially the double-passage vortexes. The mechanism for the changes of flow fields during double-slot endwall suction in the cascade remains unclear. As such, the double-slot suction schemes were investigated. The suction mass flow rate of each suction slot was 0.85% of the inlet mass flow of the baseline cascade. The influence of different suction mass flow rates was also investigated.

Figure 18 shows the suction surface/endwall limiting streamlines and static pressure contours after double-slot endwall boundary layer suction. Compared with baseline cascade, the static pressure near the suction slots increases because the reduced endwall boundary layer increases the local aerodynamic area. However, the corner open separation increases. The corner separation line originates from a saddle point S2. The saddle point S3 and node point N2 on the corner surface move toward the endwall.

The limiting streamlines in the separation region of baseline cascade flow toward the endwall, which indicates the low-momentum fluid migrates to the endwall. After double-slot suction, this trend enhances because endwall suction reduces the cross-passage pressure gradient. Thus, the low-momentum fluid does not have sufficient driving force to migrate along the blade span.

Figure 19 illustrates the loss coefficient contours at different axial sections and 3D streamlines in the corner. The suction slots remove the high loss fluid near the slots but minimally influence the corner loss distribution. The corner open separation almost remains unchanged.

Figure 20 shows the velocity vector and Mach number contours at cascade outlet. The Mach number contour is similar with ESB and ESC endwall suction schemes. As the endwall boundary layer is removed and the cross-passage pressure gradient is reduced by suction, the cross-passage flow near the endwall reduces. Thus, the torsion of the low Mach number region reduces, resulting in disappearance of the passage vortex. Only an enlarged concentration shedding vortex is found at cascade outlet.

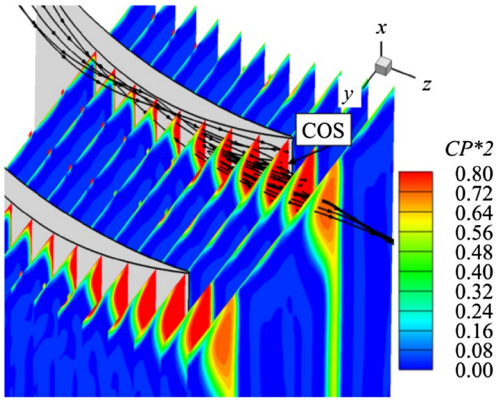

Figure 19 Loss coefficient contours & 3D streamlines

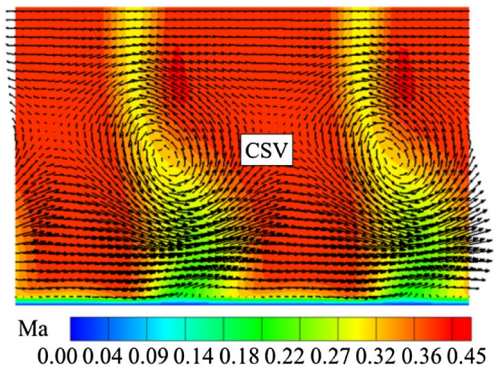

Figure 20 Velocity vector/Mach number contour

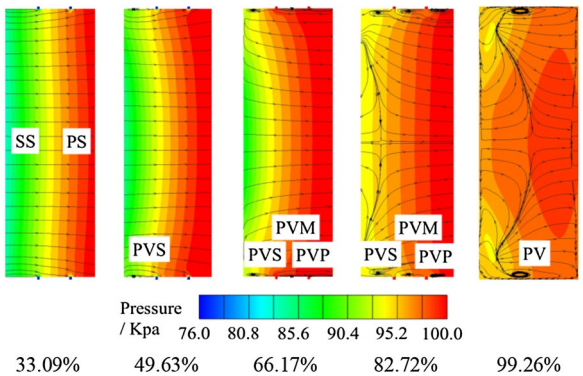

Figure 21 Static pressure contour/streamlines of different axial chords after double-slot suction

The static pressure contour/streamlines of different axial sections after ESBC suction is shown in Figure 21. ESBC suction scheme has one more suction slot near the pressure surface than ESB single suction scheme. As PVP of ESB scheme is larger than PVS, the suction slot near the pressure surface of ESBC scheme is not able to suck off the low-momentum fluid nearby. The PVP of ESB scheme is further divided into two different passage vortexes, named PVM and PVP separately. So there are three passage vortexes in the ESBC suction scheme in all. As the double-slot endwall suction sucks off more low-momentum fluid near the endwall, the onset position of the passage vortexes moves downstream and the passage vortexes are smaller than those in the ESB suction scheme. The triple-passage vortexes are clearly seen in 82.72% axial chords. The triple-passage vortexes also combine into a single-passage vortex near the cascade trailing edge. As the single-passage vortex flows downstream, it disappears during dissipation (Figure 20).

Two different suction mass flow rates were also conducted for the double-slot suction scheme to investigate

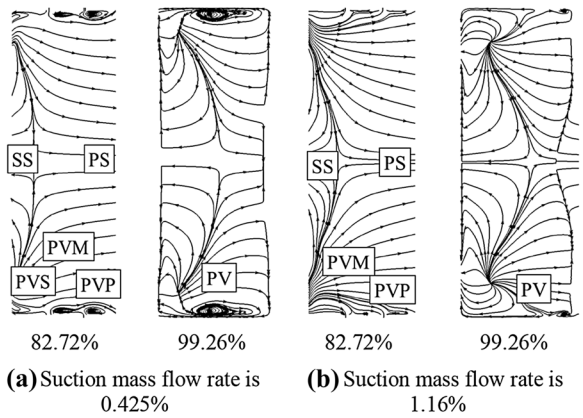

Figure 22 Comparison of streamlines at different axial chords for different suction mass flow rate

the influence of different suction mass flow rates on the flow structures; the suction mass flow rates were 0.425% and 1.16%, respectively. The overall suction mass flow rates for the double-slot scheme were 1.00, 2.00 and 2.73 times of the single-slot suction schemes.

Figure 22 shows the streamlines on typical axial chord sections for the two suction mass flow rates conditions. Figure 22(a) exhibits more severe passage vortexes than that in Figure 21, e.g., PVS, PVM and PVP at 82.72% axial chord are larger. The triple-passage vortexes also combine into a single-passage vortex near the cascade trailing edge, which is shown in Figure 22(a) at 99.26% axial chord section. The single-passage vortex is also larger than that in Figure 21. The passage vortexes are much smaller with higher suction mass flow rate, as shown in Figure 22(b). With more low-momentum fluid removed by boundary layer suction, the triple-passage vortex is smaller than that in Figure 21 and Figure 22(a). The single-passage vortex near the trailing edge is also reduced.

5.3 Flow Models of Diffusion Cascade with/without Endwall Suction

Flow models of the diffusion cascade with/without endwall suction were established, and are shown in Figure 23. Figure 23(a) shows the flow model of the baseline cascade, which mainly consists of trailing edge separation, 3D corner separation, horseshoe vortex, passage vortex, concentration shedding vortex (CSV), and corner vortex (CV). The pressure side leg of horseshoe vortex system moves toward the suction surface corner under the cross-passage pressure gradient, and it grows by sweeping-up the majority of the inlet boundary layer fluid. The 3D corner separation forms once the low energy fluids arriving at the suction surface. The low-momentum fluid on the endwall migrates toward the suction surface

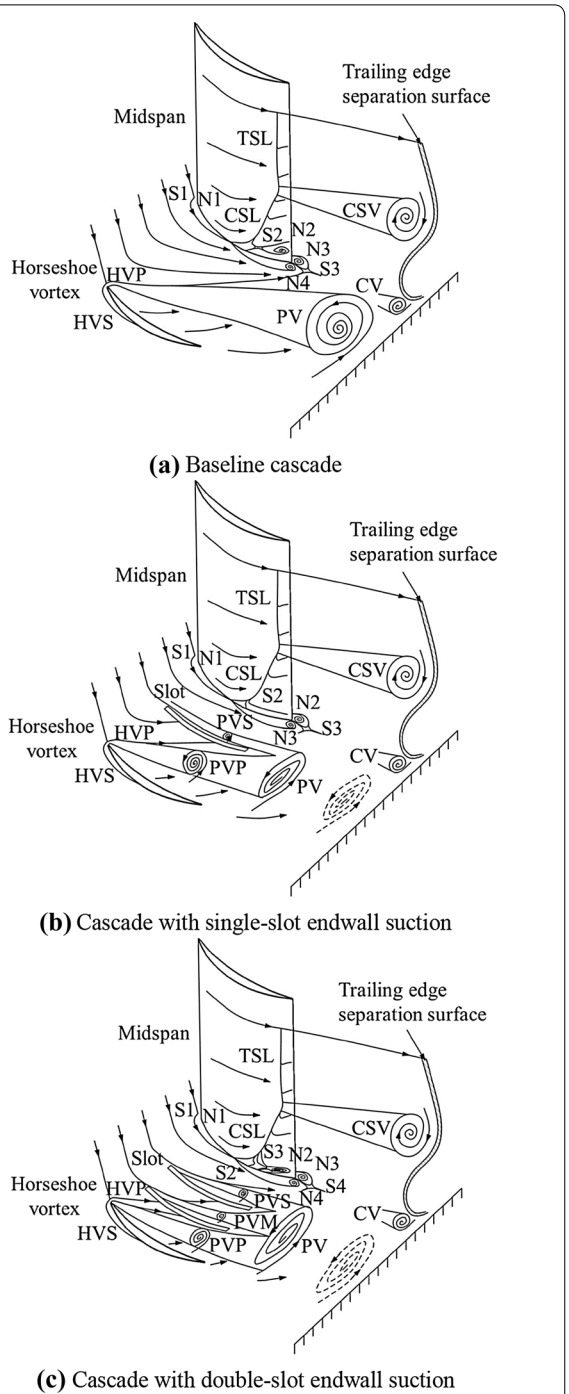

Figure 23 Flow models of diffusion cascade

and rolls up under the cross-passage pressure gradient, which results in the formation of the passage vortex. The 3D corner separation and trailing edge separation sheds together, which forms the concentration shedding vortex. Downstream of the blade trailing edge, there is a trailing edge separation surface, or called wake region. The corner vortex is a small vortex in the suction surface and endwall corner [31].

Figure 23(b) shows the flow model of the cascade with single-slot endwall suction. Only the suction slot near the middle pitchwise of the passage is presented. The HS of the leading edge horseshoe vortex moves under the endwall cross-passage pressure gradient and intersects with the suction surface soon, which is the same with baseline cascade. Compared with baseline cascade, HP is sucked off by the endwall suction slot and does not migrate to the suction surface/endwall corner. The major difference between single-slot endwall suction and baseline cascade is the double passage vortexes system. The classical passage vortex is divided into two smaller passage vortexes with single-slot endwall suction. The low-momentum fluid between pressure surface and suction slot migrates toward the suction slot under the cross-passage static pressure gradient, resulting in the formation of PVP. The endwall cross-passage flows between suction slot and suction surface reform, which forms the PVS. As PVP and PVS flow downstream, they combine into a single-passage vortex near the trailing edge section of the cascade. As the majority of the low energy fluid on the endwall is sucked off, and the cross-passage pressure gradient is reduced, the passage vortex dissipates more quickly while flowing downstream.

Figure 23(c) shows the triple-passage vortexes flow model of the double-slot endwall suction scheme. The cross-passage pressure gradient between the pressure surface and the suction slot which adjacent to the pressure surface drives the low-momentum fluid flow toward the suction surface, resulting the PVP. The PVM and PVS forms similarly. The triple-passage vortexes combine into a single-passage vortex near the trailing edge section of the cascade. The passage vortex also disappears at cascade outlet.

6 Conclusions

(1) The single-slot endwall suction scheme adjacent to the suction surface can effectively remove the corner separation. The static pressure rise coefficient of the cascade increases by 3.2% after the endwall suction. However, the trailing edge separation in the mid-span increases in that the overall diffusion of the cascade increases. The concentration shedding vortex reduces whereas the passage vortex increases.

(2) The single-slot suction schemes near the middle pitchwise of the passage divide the passage vortex into two smaller passage vortexes, which converge into a single-passage vortex near the trailing edge section of the cascade. As the endwall suction

reduces both the low energy fluid and cross-passage pressure gradient on the endwall, the passage vortex reduces. The concentration shedding vortex increases because of the increased low energy fluid in the corner.

(3) After endwall suction by double-slot suction scheme, the overturning of near endwall flow decreases because of the removal of low energy fluid and the reduction of cross-passage pressure gradient. Triple passage vortexes were found, which converge into a single-passage vortex near the trailing edge section of the cascade. The concentration shedding vortex increases.

(4) Flow models of aspirated compressor cascade were established, which shows the distinct vortexes, particularly the multi-passage-vortexes, with the traditional compressor cascade. They will contribute to the design system of future aspirated compressors.

Authors' Contributions

Z-YC was in charge of the whole trial; Z-YC wrote the manuscript; BL and TZ assisted with sampling and laboratory analyses. All authors read and approved the final manuscript.

Author details

[1] School of Power and Energy, Northwestern Polytechnical University, Xi'an 710072, China. [2] College of Engineering, Peking University, Beijing 100871, China. [3] Aero Engine Corporation of China, Xi'an Aero-engine Controls Co., Ltd, Xi'an 710077, China.

Authors' Information

Zhi-Yuan Cao, born in 1985, is currently an associate professor at *School of Power and Energy, Northwestern Polytechnical University, China*. His research interests include flow control in axial-flow compressors.

Bo Liu, born in 1960, is currently a professor at *Northwestern Polytechnical University, China*. His research interests include advanced axial-flow compressor design.

Ting Zhang, born in 1986, is currently an engineer at *Xi'an Aero-engine Controls Co., Ltd, China*. Her research interests include design and optimization of fluid machinery.

Competing Interests

The authors declare that they have no competing interests.

Funding

Supported by China Postdoctoral Science Foundation (Grant No. 2016M600015), and National Natural Science Foundation of China (Grant Nos. 51741601, 51236006).

Publisher's Note

Received: 2 January 2016 Accepted: 5 June 2018
Published online: 19 June 2018

References

[1] Members of the staff of Lewis Research Center. *Aerodynamic design of axial-flow compressors, revised*. Washington, D. C.: NASA Report, 1965, No. NASA SP–36.

[2] A J Wennerstrom. Highly loaded axial flow compressors: history and current developments. *Journal of Turbomachinery*, 1990, 112(4): 567–578.

[3] Dickens Tony, Day Ivor. The design of highly loaded axial compressors. *Journal of Turbomachinery*, 2011, 133(3): 031007–1–10.

[4] Ya-Ping Ju, Chu-Hua Zhang. Robust design optimization method for centrifugal impellers under surface roughness uncertainties due to blade fouling. *Chinese Journal of Mechanical Engineering*, 2016, 29(2): 301–314.

[5] Ji Pei, Wen-Jie Wang, Shou-Qi Yuan, et al. Optimization on the impeller of a low-specific-speed centrifugal pump for hydraulic performance improvement. *Chinese Journal of Mechanical Engineering*, 2016, 29(5): 992–1002.

[6] C Beselt, M Eck, D Peitsch. Three-dimensional flow field in highly loaded compressor cascade. *Journal of Turbomachinery*, 2014, 136(3): 101007–1–10.

[7] Ya-Ping Ju, Hui Liu, Zi-Yuan Yao, et al. Fluid-structure interaction analysis and lifetime estimation of a natural gas pipeline centrifugal compressor under near-choke and near-surge conditions. *Chinese Journal of Mechanical Engineering*, 2015, 28(6): 1261–1268.

[8] K Auchoybur, R J Miller. Design of compressor endwall velocity triangles. *Proceedings of the ASME Turbo Expo 2016: Turbomachinery Technical Conference and Exposition*, Seoul, South Korea, June 13–17, 2016: GT2016–57396.

[9] Yang-Wei Liu, Hao Yan, Li-Peng Lu, et al. Investigation of vortical structures and turbulence characteristics in corner separation in a linear compressor cascade using DDES. *Journal of Fluids Engineering*, 2017, 139(2): 021107.

[10] J V Taylor, R J Miller. Competing 3D mechanisms in compressor flows. *Proceedings of the ASME Turbo Expo 2015: Turbine Technical Conference and Exposition*, Montreal, Quebec, Canada, June 15–19, 2015: GT2015–43322.

[11] J L Keerebrock, D P Reijnen, W S Ziminsky, et al. Aspirated compressors. *Proceedings of the ASME Turbo Expo 1997: International Gas Turbine and Aeroengine Congress and Exhibition*, Orlando, Florida, USA, June 2–5, 1997: 97–GT–925.

[12] J L Keerebrock. The prospects for aspirated compressors. *Proceedings of the AIAA Fluids 2000 Conference and Exhibit*, Denver, Co, USA, June 19–22, 2000: AIAA–2000–2472.

[13] A Merchant, J L Kerrebrock, A Epstein. Compressors with aspirated flow control and counter-rotation. *Proceedings of the 2nd AIAA Flow Control Conference*, Portland, Oregon, June 28–July 1, 2004: AIAA–2004–2514.

[14] A Merchant. Aerodynamic design and performance of aspirated airfoils. *Journal of Turbomachinery*, 2003, 125(1): 141–148.

[15] B J Schuler, J L Kerrebrock, A Merchant. Experimental investigation of a transonic aspirated compressor. *Journal of Turbomachinery*, 2005, 127(2): 340–348.

[16] A Merchant, J L Kerrebrock, J J Adamczyk, et al. Experimental investigation of a high pressure ratio aspirated fan stage. *Journal of Turbomachinery*, 2005, 127(1): 43–51.

[17] Power Bronwyn, Li-Ping Xu, Wellborn Steven. Numerical and experimental findings of a highly-loaded aspirated cascade. *Proceedings of the ASME Turbo Expo 2014: Turbine Technical Conference and Exposition*, Dusseldorf, Germany, June 16–20, 2014: GT2014–27098.

[18] Yang-Wei Liu, Jin-Jing Sun, Li-Peng Lu. Corner separation control by boundary layer suction applied to a highly loaded axial compressor cascade. *Energies*, 2014, 7(12): 7994-8007.

[19] Zhi-Yuan Cao, Bo Liu, Ting Zhang, et al. Influence of coupled boundary layer suction and bowed blade on flow field and performance of a diffusion cascade. *Chinese Journal of Aeronautics*, 2017, 30(1): 249–263.

[20] Song-Tao Wang, Xiao-Qing Qiang, Wei-Chun Lin, et al. Highly-loaded low-reaction boundary layer suction axial flow compressor. *Proceedings of the ASME Turbo Expo ASME Turbo Expo 2007: Power for Land, Sea, and Air*, Montreal, Canada, May 14–17, 2007: GT2007–28191.

[21] Xiao-Qing Qiang, Song-Tao Wang, Weichun Lin, et al. A new design concept of highly-loaded axial flow compressor by applying boundary layer suction and 3D blade technique. *Proceedings of the ASME Turbo Expo ASME 2008 International Mechanical Engineering Congress and Exposition*, Boston, Massachusetts, USA, October 31–November 6, 2008: IMECE2008–66899.

[22] Fu Chen, Yan-Ping Song, Huan-Long Chen, et al. Effects of boundary layer suction on the performance of compressor cascades. *Proceedings of the ASME Turbo Expo 2006: Power for Land, Sea, and Air*, Barcelona, Spain, May 8–11, 2006: GT2006–90082.

[23] Yan-Ping Song, Fu Chen, Jun Yang, et al. A numerical investigation of boundary layer suction in compound lean compressor cascade. *Proceedings of the ASME Turbo Expo 2005: Power for Land, Sea, and Air*, Reno, Nevada, USA, June 6–9, 2005: GT2005–68441.
[24] S A Gbadebo, N A Cumpsty, T P Hynes. Three-dimensional separations in axial compressors. *Journal of Turbomachinery*, 2005, 127(2): 331–339.
[25] S A Gbadebo. *Three-dimensional separations in compressors*. Cambridge: University of Cambridge, 2003.
[26] S A Gbadebo, N A Cumpsty, T P Hynes. Control of three-dimensional separations in axial compressors by tailored boundary layer suction. *Journal of Turbomachinery*, 2008, 130(1): 011004–1–8.
[27] Ping-Ping Chen, Wei-Yang Qiao, Liesner Karsten, et al. Location effect of boundary layer suction on compressor hub-corner separation. *Proceedings of the ASME Turbo Expo 2014: Turbine Technical Conference and Exposition*, Dusseldorf, Germany, June 16–20, 2014: GT2014–25043.
[28] Zhi-Yuan Cao, Bo Liu, Ting Zhang. Control of separations in a highly loaded diffusion cascade by tailored boundary layer suction. *Proceedings of the Institution of Mechanical Engineers, Part C: Journal of Mechanical Engineering Science*, 2013, 228(8): 1363–1374.
[29] NUMECA International. *User Manual-FINETM/Turbo v8.7*. Brussel: NUMECA International, 2009.
[30] S J Decook. *Expermental investigation of trailing edge crenulation effects on losses in a compressor cascade*. Ohio: AD Report, 1991, No. AD–A243 902.
[31] Shun Kang. *Investigation of the three dimensional flow within a compressor cascade with and without tip clearance*. Brussel: Vrije Universiteit, 1993.